Ultralow-power second-harmonic generation frequency-resolved optical gating using aperiodically poled lithium niobate waveguides [Invited]

Houxun Miao,[1,*] Shang-Da Yang,[2] Carsten Langrock,[3] Rostislav V. Roussev,[3] M. M. Fejer,[3] and Andrew M. Weiner[1]

[1]*Purdue University, West Lafayette, Indiana 47907, USA*
[2]*National Tsing-Hua University, Hsinchu 30013, Taiwan*
[3]*E. L. Ginzton Laboratory, Stanford University, Stanford, California 94305, USA*
**Corresponding author: hmiao@purdue.edu*

Received December 17, 2007; accepted January 27, 2008;
posted February 25, 2008 (Doc. ID 90881); published April 22, 2008

We discuss ultralow-power second-harmonic generation (SHG) frequency-resolved optical gating (FROG) in the telecommunication C-band using aperiodically poled lithium niobate (A-PPLN) waveguides as the nonlinear medium. A key theme of this work is that the phase-matching curve of the nonlinear medium is engineered to obtain an optical bandwidth adequate for measurement of subpicosecond pulses while retaining the optimum nonlinear efficiency consistent with this constraint. Our experiments demonstrate measurement sensitivity (defined as the minimum product of the peak and average pulse powers at which a reliable nonlinear signal can be detected) of 2.0×10^{-6} mW^2 in a collinear SHG FROG geometry, approximately 5 orders of magnitude better than previously reported for any FROG measurement modality. We also discuss asymmetric Y-junction A-PPLN waveguides that permit background-free SHG FROG and a polarization-insensitive SHG FROG technique that eliminates the impairment that frequency-independent random polarization fluctuations induce in the FROG measurement. Finally, we applied these SHG FROG techniques in chromatic dispersion and polarization mode dispersion compensation experiments. In these experiments the FROG data enabled complete correction of distortions incurred by subpicosecond pulses passing through optical fibers; these results also demonstrate the ability to retrieve extremely complex pulses with high accuracy.

OCIS codes: 320.7100, 130.3730, 320.5540, 260.5430.

1. INTRODUCTION

The applications of ultrafast optics in various fields, such as studies of molecular vibrations [1], new types of spectroscopy [2], and optical code-division multiple-access light-wave communication systems [3], depend critically on the capability to fully characterize ultrashort optical pulses. A number of methods have been proposed and demonstrated for the complete characterization of the amplitude and phase profiles of ultrashort pulses, which can be grouped into three main categories: spectrography, tomography, and interferometry. Among these methods, the two most popular ones are frequency-resolved optical gating (FROG, spectrography) [4–10] and spectral phase interferometry for direct electric-field reconstruction (SPIDER, interferometry) [11–15]. Nonlinear optical interactions are widely used in ultrashort pulse measurement techniques. For example, polarization-gate FROG uses the electronic Kerr effect, second-harmonic generation (SHG) FROG uses a $\chi^{(2)}$ process, self-diffraction FROG uses a third-order nonlinear optical process, SPIDER typically uses a $\chi^{(2)}$ nonlinearity, etc. Even when using crystals with large nonlinear coefficients, the conversion efficiencies of nonlinear interactions are typically low. As a result, the best measurement sensitivity (defined as the minimum product of the peak and average pulse powers at which a reliable nonlinear signal can be detected) of multishot SHG FROG using bulk SHG crystals (considered the most sensitive of the traditional FROG geometries) is $\sim$500 mW^2 [16]. The difficulty in measuring ultraweak pulses limits the applications of ultrafast optics in certain ultrafast nonlinear optical material characterization methods and often in experimental ultrafast light-wave communications.

A focus of our work is to bring sophisticated ultrafast optical measurement techniques into light-wave technology practice. To enable light-wave applications, several challenging requirements must first be met that are not usually encountered in ultrafast optics. In addition to the obvious wavelength requirement, a fundamental research challenge involves the pursuit of orders-of-magnitude improvement in nonlinear optical sensitivity, which is desirable in order to adapt sophisticated ultrafast optical measurement techniques to the low power levels and very high repetition rates typical of practical light-wave systems. For example in light-wave dispersion monitoring applications, monitoring should tap off less than 1%–3%

of the transmitted power, and the detection response should be faster than the time scale of dispersion variation (~100 ms) to support real-time performance recovery [17]. This requires operation at average powers in the microwatt regime and possibly below.

In our previous work [18,19], by using aperiodically poled lithium niobate (A-PPLN) waveguides as the nonlinear medium, we demonstrated ultralow-power multishot SHG FROG in the telecommunication band with a measurement sensitivity of 2.0×10^{-6} mW^2, an 8 order of magnitude improvement over SHG FROG using bulk crystals and 5 orders of magnitude better than previously reported for any FROG measurement modality [20]. This improved sensitivity allowed high-quality pulse measurements at nanowatt to tens of nanowatt average power of subpicosecond pulses with a 50 MHz repetition rate. Additionally, some of us have designed and demonstrated asymmetric Y-junction A-PPLN waveguides that result in a background-free SHG FROG setup [21] (in contrast to most of the measurements reported here, in which a background must be removed by software).

We further developed a polarization-insensitive SHG FROG technique [22] by scrambling the polarization of the pulse under test much faster than the measurement integration time. This technique eliminates the impairment that frequency-independent random polarization fluctuations induce in the FROG measurements (since in general, the nonlinear response is strongly polarization dependent) and enables robust FROG measurements without taking special care of polarization fluctuations induced by the single-mode fibers (SMFs) in the FROG setup. Such polarization insensitivity is very important for many applications in fiber optics, where in general polarization is not stable.

Finally, we have applied the ultralow-power SHG FROG technique to characterize distortions encountered by subpicosecond pulses due to chromatic dispersion and polarization mode dispersion (PMD) in optical fibers. Furthermore, we have used the FROG data to control waveform compensation experiments implemented by using liquid-crystal-modulator-based pulse shapers [23–25]. Essentially complete waveform compensation is achieved for both chromatic dispersion and PMD. Such compensation experiments both extend the range of fiber over which subpicosecond pulses may transmitted and confirm that our SHG FROG measurements provide reliable information.

This paper reviews ultralow-power SHG FROG using A-PPLN waveguides and its applications in ultrafast optics. In Section 2, we explain the basic measurement principles with an emphasis on the role of the phase-matching response. In Section 3, we describe the design and fabrication of A-PPLN waveguides. In Sections 4–6 we review SHG FROG experiments with free-space A-PPLN, fiber-pigtailed A-PPLN, and asymmetric Y-junction A-PPLN waveguides, respectively. In Section 7, we introduce polarization-insensitive SHG FROG. In Section 8, we demonstrate the applications of the proposed techniques in chromatic dispersion compensation and all-order PMD compensation. Finally, in Section 9, we conclude this paper.

2. MEASURMENT PRINCIPLES

SHG has long been the most popular nonlinear process used for pulse measurement in the field of ultrafast optics [26]. For many years the intensity autocorrelation function, which provides useful (but incomplete) information about the duration of ultrashort pulse intensity profiles, was the standard measurement tool. Briefly, an input pulse is split in two, given a relative delay, and then recombined to form a pulse pair that interacts in a SHG crystal. Because SHG is a nonlinear process, the time-integrated second-harmonic (SH) power is higher when the relative delay is less than the pulse duration. Recording the average SHG power with a slow powermeter, as a function of relative delay, yields the intensity autocorrelation function. FROG goes well beyond the intensity autocorrelation to provide measurement of the complete phase and amplitude profiles of ultrashort pulses. The setup for FROG measurements based on SHG are similar to those for intensity autocorrelation, except that a spectrometer is placed after the SHG crystal and prior to the detector. Recording the average by SHG power as a function both of delay and SH frequency provides a rich two-dimensional data set, which can be analyzed by using iterative computer techniques for essentially complete reconstruction of the pulse under test [4].

In bulk SHG crystals, the conversion efficiency is restricted in part by the Gaussian beam diffraction, which prevents the coexistence of a small interaction area and a long interaction length. By formatting the guiding structure on lithium niobate (LN) substrates, we tightly confine the optical beam over a long interaction distance, which provides a significant increase in conversion efficiency. Temporal resolution in ultrafast optical measurements involving SHG is usually limited by the group-velocity mismatch (GVM) between fields at the fundamental frequency and the SH frequency. The effect of velocity mismatch is to broaden the generated SH pulse in proportion to the GVM and to limit the phase matching necessary for an efficient nonlinear interaction to a narrow range of SH frequencies, with bandwidth proportional to GVM^{-1} (here and below, we use "GVM" to refer to the total temporal walk-off in picoseconds). Measurement distortions arising from excessive GVM and insufficient phase-matching bandwidth were first studied by Weiner for autocorrelations [27] and later by Trebino and coworkers for FROG [10]. Mathematically, the finite phase-matching bandwidth introduces an undesired filter function H(Ω), the effect of which can be seen in Eqs. (1)–(4):

$$I_{\mathrm{FROG}}(\Omega,\tau)\sim\left|\int \mathrm{d}tE(t)E(t-\tau)e^{-j\Omega t}\right|^2, \tag{1}$$

$$I'_{\mathrm{FROG}}(\Omega,\tau)\sim|H(\Omega)|^2I_{\mathrm{FROG}}(\Omega,\tau), \tag{2}$$

$$G_2(\tau)\sim\int \mathrm{d}t|E(t)E(t-\tau)|^2\sim\int \mathrm{d}\Omega I_{\mathrm{FROG}}(\Omega,\tau), \tag{3}$$

$$G'_2(\tau)\sim\int \mathrm{d}\Omega I'_{\mathrm{FROG}}(\Omega,\tau), \tag{4}$$

where Eqs. (1) and (2) show the SHG FROG traces without and with GVM and Eqs. (3) and (4) show the autocor-

relation traces without and with GVM. To obtain an accurate measurement, the GVM is usually made less than the coherence time of the signal of interest, which is equivalent to requiring that the phase-matching bandwidth for SHG exceed the optical bandwidth. This condition is usually met by reducing the length of the nonlinear crystal (sometimes to only tens of micrometers), which reduces the GVM, but with a corresponding sacrifice in efficiency. For typical ultrafast optics applications where fairly high intensities are available (typically pulse energies up to a few nanojoules for 100 MHz mode-locked laser oscillators and up to 1 mJ for 1 KHz femtosecond amplifier systems), the loss of SHG efficiency is usually not serious. However, in the context of applications to lightwave systems, average powers are usually low and repetition rates are high (e.g., 10 GHz and above), which means that sensitivity is desired for pulse energies in the picojoule and femtojoule range and below. Optimizing the nonlinear optical efficiency then becomes a key concern. In our work, we have addressed this issue by utilizing SHG waveguide devices (A-PPLN waveguides), which are modified to provide broad SHG phase-matching bandwidth simultaneously with the long interaction lengths necessary for high efficiency and sensitivity.

As explained above, adequate phase-matching bandwidth in SHG is usually achieved by reducing the length of the nonlinear crystal, which reduces the GVM. Compared with a long crystal of length L, in a short crystal of length L/N the phase-matching bandwidth is increased by a factor N. However, as sketched in Fig. 1, the peak efficiency drops by N^2, which means that there is a large cost in sensitivity (Gaussian beam diffraction is not taken into account here). A much more favorable trade-off, which is the key to our work, is possible by staying with a long crystal but chirping the quasi-phase-matched (QPM) grating to broaden the bandwidth. For a factor of N broadening of the phase-matching bandwidth, now the peak efficiency drops only by N, which is the best that can be achieved. Given that a 6 cm PPLN waveguide has ~20 ps GVM, and assuming a temporal resolution goal of 200 fs, the long chirped crystal is 2 orders of magnitude more efficient than the short unchirped crystal. This advantage comes on top of the dramatic increase in efficiency compared with bulk media that is available even with short channel waveguides.

It is interesting to note that although the proposed QPM chirp does indeed increase the phase-matching bandwidth, it does not eliminate or even reduce GVM. The key but subtle point is that although measurement accuracy in pulse measurements such as SHG autocorrelation and FROG really does depend on the phase-matching bandwidth [27], there is fundamentally no requirement that the GVM in the time domain be made small. In fact, it is not even required that all the frequencies be phase matched simultaneously; only the phase-matching bandwidth integrated over the measurement needs to exceed the optical signal bandwidth [28,29]. This concept has been exploited to perform FROG in a thick SHG crystal with a tightly focused beam, where different SH frequencies are phase matched at different output angles [28], or in a frequency-swept scheme where the angle of the SHG crystal is dithered in order to sweep the phase-matching frequency [29]. In our work different SH frequencies are generated at different longitudinal locations within a single chirped QPM waveguide and impinge on a single detector, an arrangement that leads to extremely high sensitivity. With reference to Eqs. (1)–(4), our scheme results in a phase-matching filter function whose magnitude $|H(\Omega)|$ is approximately flat. The phase of $H(\Omega)$ will show strong frequency variation, but this does not affect the pulse measurement.

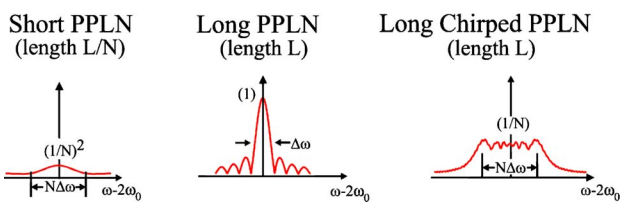

Fig. 1. (Color online) Chirped QPM gratings allow tailoring of upconversion bandwidth, needed for accurate pulse measurements, while maintaining maximum efficiency consistent with the bandwidth requirement.

3. A-PPLN WAVEGUIDES

The fabrication of QPM waveguide devices on ferroelectric substrates, such as the reverse-proton-exchanged (RPE) periodically poled lithium niobate (PPLN) waveguides used in this paper, can be divided into two independent processes, the generation of the QPM grating via periodic ferroelectric domain inversion of the substrate, and the formation of the guiding structure, typically by an ion-exchange process. Our choice of LN as the substrate for the fabrication of guided-wave nonlinear optical devices is motivated by several factors. To achieve efficient frequency conversion in nonlinear optical processes, such as the SHG used in this paper, we require the material of choice to have as large a nonlinear coefficient as possible. Furthermore, the material must be transparent at all wavelengths involved in the nonlinear interaction. LN, with its transparency between 325 and 4500 nm and nonlinear coefficient $d_{33}=27$ pm/V (among the largest of any ferroelectric material), is a good choice for telecommunication applications.

As described in [30], QPM allows us to engineer the nonlinear response of a given material, largely independent of its dispersive or crystallographic properties. To achieve this control, the sign of the nonlinear susceptibility has to be inverted either periodically or aperiodically. Ferroelectric materials make this task rather straightforward through the inversion of the ferroelectric domains via an externally applied electric field [31]. Since this domain inversion also inverts the nonlinear susceptibility tensor, domain inversion is equivalent to changing the sign of the second-order nonlinear susceptibility $\chi^{(2)}$.

We used apodized A-PPLN waveguides [32] for the experiments described in this paper. The aperiodicity of the QPM grating refers to the change in local periodicity as a function of position along the waveguide. Unlike the conversion bandwidth of a periodic (i.e., uniform) QPM grating, which is inversely proportional to the length of the grating (e.g., 0.25 nm FWHM for a 5 cm long grating for a 1.5 μm fundamental wavelength), the bandwidth of a lin-

early chirped grating is determined by the chirp parameter [33,34]. Tens of nanometers of conversion bandwidth are easily obtainable and make nonlinear frequency conversion of large-bandwidth pulses possible. Furthermore, it has been shown that it is also possible to engineer the phase response of QPM gratings (not used here, since phase does not matter in the measurement of SHG spectra in FROG), for example to shape SH pulses [35]. We used the deleted-reversal apodization technique described in [32] to engineer QPM gratings with 25 nm wide flat passbands for the experiments presented in Sections 5 and 6. By apodization, we mean to smooth the discontinuities of the nonlinearity at the beginning and end of the QPM grating to achieve a flattened phase-matching curve. As an example, Fig. 2 shows the phase-matching curves of a PPLN waveguide and an apodized A-PPLN waveguide. Note that the SHG efficiency for a pulse of a given energy in an A-PPLN waveguide remains nearly the same as that of a PPLN waveguide of the same length as long as the phase-matching bandwidth is not significantly broader than the input spectrum [36].

Equally important for our substrate choice is the availability of low-loss nonlinear waveguides in LN. Because of LN's favorable properties for three-wave mixing, researchers have investigated the implementation of guided-wave structures, which provide a significant increase in conversion efficiency (2–3 orders of magnitude) due to tight modal confinement over appreciable length of nonlinear interaction. Several waveguide fabrication methods have been developed, such as annealed proton exchange [37], titanium indiffusion [38], RPE [39–42], and ridge waveguide formation by mechanical sawing or chemical etching [43,44].

Here, we will concentrate on the fabrication of protonated waveguides used for the experiments described in this paper. After electric-field-assisted domain inversion, channels are lithographically defined along the crystallographic y direction through a silicon dioxide mask patterned photlithographically in a film sputtered on the $+z$ side of the wafer. When the wafer is placed into a heated acid bath (here, benzoic acid), hydrogen ions are exchanged with lithium ions in the channels. A high-temperature annealing step subsequantly drives the protons deeper into the substrate, reducing the propagation losses by pushing the propagating fields farther from the substrate surface (0.2–0.4 dB/cm typically). This type of waveguide is called an annealed-proton-exchange waveguide. By an additional exchange step in a lithium-rich melt, the asymmetric annealed-proton-exchange index profile can be somewhat symmetrized by replacing protons by lithium ions in the top layer of the waveguiding structure [41,45]. The resulting waveguide has been termed a RPE waveguide. This RPE step further increases the separation between the propagating fields and the substrate surface, reducing surface scattering. State-of-the-art efficient nonlinear RPE waveguides have propagation losses $\leqslant$0.1 dB/cm.

The outlined fabrication process does not restrict us to the implementation of purely straight waveguide structures. While these are the most common components found in wavelength converters, additional functionality can be achieved by adding more sophisticated integrated structures, such as adiabatic tapers, required for low-loss and stable coupling to SMF [46]. To avoid excitation of higher-order modes of the multimoded QPM region, a so-called mode filter, essentially a single-mode waveguide section a few millimeters long, is often added in front of the taper. The proper design of such structures requires accurate models of the concentration-dependent proton diffusion and the resulting wavelength-dependent refractive index [47,48].

Since protonated waveguides support only a single polarization (TM), type II mixing processes are not possible, and so autocorrelation or FROG measurements using these devices will exhibit background SH and interferometric effects. (In Sections 4 and 5, we will show how to externally reduce these impairments). With the help of on-chip mode multiplexer–demultiplexers (here, asymmetric Y-junctions) in combination with two-mode RPE PPLN waveguides [49,50] as shown in Fig. 3, one can significantly reduce the interferometric oscillations and almost completely suppress the background. The principle behind this can be understood as follows. One of the inputs (Signal 1 in Fig. 3) is launched into the TM_{10} mode, while the other one (Signal 2) is launched into the TM_{00} mode. The sum-frequency generation (SFG) between these two spatial modes is generated in the TM_{10} mode, while the SH of each input appears in an even-order mode, TM_{20} or TM_{00}, resembling a type II birefringently phase-matched interaction. By using a mode demultiplexer at the output of the waveguide, the SFG component can be separated from the SH components, resulting in a collinear but background-free interaction. Given ideal device performance, the SFG autocorrelation trace and SFG FROG data are identical to those obtained with conventional background-free methods, while the large nonlinear conversion efficiency available in engineered QPM waveguide structures provides a greatly enhanced measurement sensitivity.

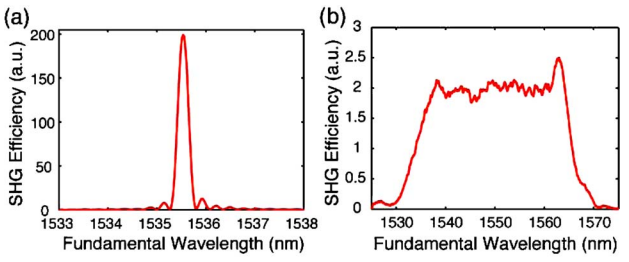

Fig. 2. (Color online) Experimental phase-matching curves of (a) PPLN and (b) apodized A-PPLN waveguides. Note the difference in scale of the abscissas in the two figures. The bandwidth of the A-PPLN is 100 times larger than that of the PPLN device.

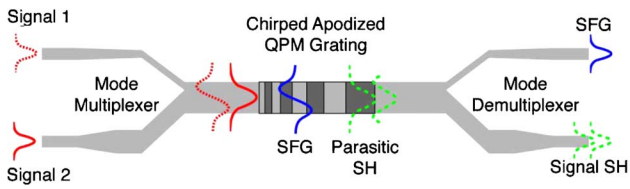

Fig. 3. (Color online) Schematic of an asymmetric Y-junction device showing mode multiplexer at the input and demultiplexer at the output. Note that an odd SH spatial mode can be generated only through mixing an even and an odd FH mode, and so contains only SFG and not SH contributions.

4. SHG FROG WITH A FREE-SPACE A-PPLN WAVEGUIDE

The setup of our SHG FROG experiments is shown in Fig. 4, where a free-space-coupled A-PPLN waveguide with a 25 nm wide phase-matching bandwidth centered at 1538 nm is used for SHG. We employ a passively mode-locked fiber ring laser [51] and a bandpass filter to generate a 50 MHz, ~280 fs pulse train at 1538 nm center wavelength. The pulse train is sent into a modified collinear Michelson interferometer, where the unwanted interferometric fringes are removed by fast dithering of the fixed arm of the interferometer, using a piezoelectric transducer [52]. The output SH power spectrum from the A-PPLN waveguide is recorded by a spectrometer and an intensified CCD camera for each delay, giving rise to a fringe-suppressed raw FROG trace, which has a nonzero background and is spectrally distorted by the somewhat uneven phase-matching spectrum of the A-PPLN waveguide. Subsequent software processing deals with (i) background subtraction, (ii) frequency marginal correction [4] (with the aid of the fundamental power spectrum taken by an optical spectrum analyzer), and (iii) intensity and phase reconstruction by commercial software (Femtosoft FROG 3).

Figure 5 illustrates measured (after background subtraction and marginal correction) and retrieved FROG traces at coupled pulse energies of 9.5 fJ [Figs. 5A and 5B] and 124 aJ [Figs. 5C and 5D] [18]. Even with a 19 dB input power difference (38 dB difference in SHG powers), these FROG traces agree well with one another. The FROG errors are 0.0022 and 0.0032, respectively. Fig. 5 also shows the retrieved pulses in [Fig. 5E] frequency and [Fig. 5F] time domains for both input power levels. An independently measured input power spectrum is plotted as a dotted curve in Fig. 5E for comparison. The retrieved spectral intensities closely approach this curve. The retrieved temporal profiles also overlap well with each other, where the intensity FWHM values are essentially identical: 279 and 278 fs. The low-power measurement is equivalent to 0.44 mW peak power, and 6.2 nW average power, corresponding to a measurement sensitivity of 2.7×10^{-6} mW^2.

We also measured optical pulses with quadratic spectral phase induced by a piece of SMF and cubic spectral phase induced by a pulse shaper, which indicate that our SHG FROG with free-space-coupled A-PPLN waveguide can correctly reconstruct fairly complex optical pulses. More details are presented in [18,52].

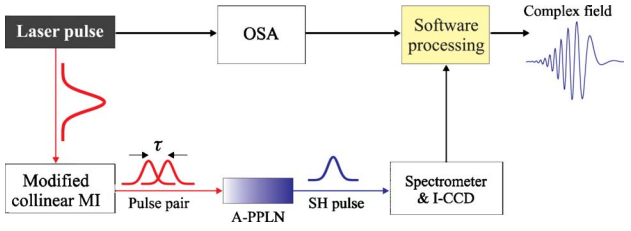

Fig. 4. (Color online) Schematic diagram of SHG FROG using an A-PPLN waveguide. MI, Michelson interferometer; OSA, optical spectrum analyzer; I-CCD, intensified CCD camera.

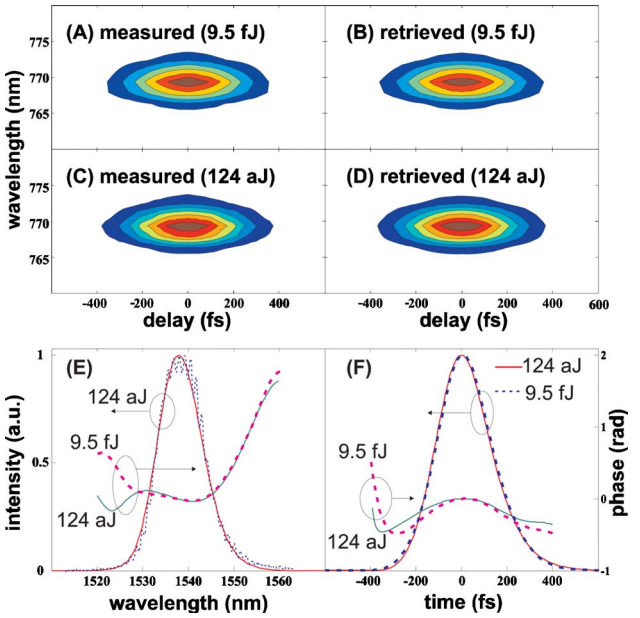

Fig. 5. (Color online) FROG data of nearly bandwidth-limited pulses. (A) Measured and (B) retrieved FROG traces at 9.5 fJ. (C) Measured and (D) retrieved FROG traces at 124 aJ. Retrieved pulse illustrated in the (E) frequency domain and (F) time domain for both 9.5 fJ and 124 aJ coupled pulse energies. The dotted curve in (E) represents the independently measured power spectrum.

5. SHG FROG WITH A FIBER-PIGTAILED A-PPLN WAVEGUIDE

The performance of the FROG setup using free-space-coupled A-PPLN waveguides is limited mainly by the time-dependent free-space-to-waveguide coupling efficiency induced by mechanical drifts. The simplest and most robust way to eliminate coupling efficiency fluctuations is to use a fiber-pigtailed A-PPLN waveguide. The design of waveguides with modes tapered to allow good fiber coupling was described in Section 3.

The FROG setup and measurement process are the same as in Section 4, except that the free-space-coupled A-PPLN waveguide is replaced by a fiber-pigtailed one. (We retain free-space coupling for the output end of the waveguide.) The center wavelength of the phase-matching curve of the fiber-pigtailed A-PPLN waveguide was 1550 nm at room temperature with a bandwidth of ~25 nm. We used a tunable bandpass filter (FWHM ~10 nm) to select ~360 fs optical pulses with a 1550 nm center wavelength from a passively mode-locked fiber ring laser operating at a 50 MHz repetition rate. We placed a phase-only pulse shaper before the FROG setup to apply a known spectral phase to the optical pulses.

We performed FROG measurements of nearly bandwidth-limited pulses (with a coupled average power of 6 nW, corresponding to a measurement sensitivity of 2.0×10^{-6} mW^2 with the 360 fs pulse width) and pulses with a cubic spectral phase of varying magnitude (with a coupled average power of 10 nW). Figures 6 and 7 show the results for the bandwidth-limited pulses and pulses with a cubic spectral phase coefficient of 0.0213 ps^3, respectively. The FROG errors for all the measurements were below 0.004. The symmetry of the FROG traces with

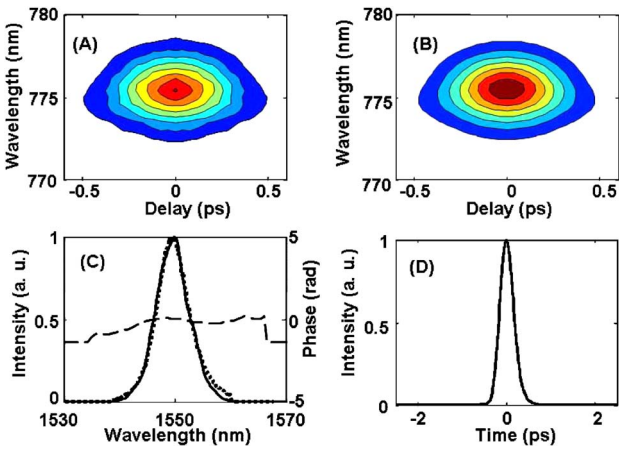

Fig. 6. (Color online) FROG data for bandwidth-limited optical pulses. (A) Measured FROG trace. (B) Retrieved FROG trace. (C) Retrieved spectral intensity (solid) and phase (dashed) profiles together with the spectrum recorded by OSA (dotted). (D) Retrieved temporal intensity profile.

respect to delay for pulses with cubic spectral phase is expected according to the time-reversal ambiguity of SHG FROG. The retrieved spectral phase was flat in the bandwidth-limited case. In the case of nonzero cubic spectral phase, the retrieved spectral phase curve is of cubic nature with an estimated coefficient of 0.0201 ps^3. The temporal intensity profile clearly shows an oscillating tail caused by the cubic spectral phase modulation. The estimated coefficient agrees well with the value programmed into the pulse shaper. By programming the pulse shaper, we repeated the FROG measurements for several values of the cubic spectral phase coefficient. In each case, the magnitude of the estimated coefficient agreed well with the programmed one. Since time reversal ambiguity exists in SHG FROG, the sign of the spectral phase cannot be determined uniquely, and the retrieved electrical fields are sometimes time reversed compared to the actual fields. By using the programmable pulse shaper, we can resolve this ambiguity by programming an additional (known) phase and performing an additional measurement.

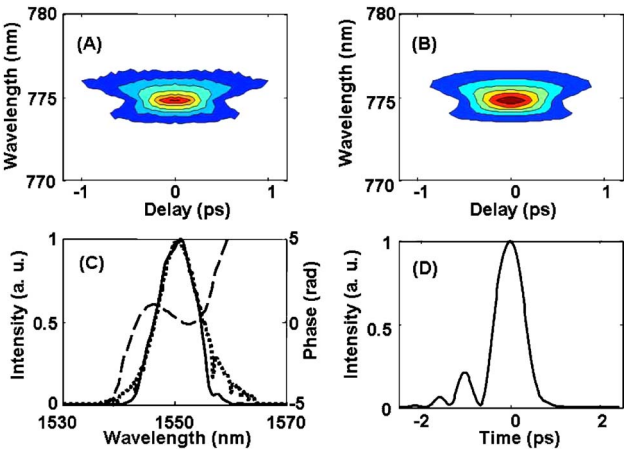

Fig. 7. (Color online) FROG data for optical pulses with cubic spectral phase. (A) Measured FROG trace. (B) Retrieved FROG trace. (C) Retrieved spectral intensity (solid) and phase (dashed) profiles together with the spectrum recorded by OSA (dotted). (D) Retrieved temporal intensity profile.

6. SHG FROG USING ASYMMETRIC Y-JUNCTION A-PPLN WAVEGUIDES

In Sections 4 and 5, single-mode A-PPLN waveguides were used in the FROG setup where the resulting background SH and interferometric effects were removed outside the waveguides. In this section, we implemented two different experimental setups to compare single-mode waveguides to mode-multiplexing ones (Fig. 8). Bandwidth-limited pulses from a synchronously pumped optical parametric oscillator (OPO) operating at 1550 nm were bandpass filtered (1 nm FWHM) and launched into SMF. With a 3 dB coupler, the pulses were split into two identical replicas, one of which was sent through a fixed delay, while the other passed through a variable delay line (General Photonics MDL-001). In the conventional setup, which uses a straight fiber-coupled A-PPLN waveguide [Setup A, Fig. 8(a)], the delayed copies were recombined in a second 3 dB splitter before being launched into the waveguide. Setup B [Fig. 8(b)] used a waveguide with an on-chip mode-multiplexer–demultiplexer. Here, the second 3 dB splitter was not required because of the integrated mode combiner (see Fig. 3). Instead, two SMFs were directly pigtailed to the inputs of the A-PPLN device. Both optical power and spectra of the SHG–SFG output were recorded as a function of relative temporal delay by using a silicon detector and fiber-coupled spectrometer (Ocean Optics HR4000).

The interferometric autocorrelation trace obtained with setup A is shown in Fig. 9(a). Assuming a Gaussian pulse envelope, the FWHM pulse duration τ_p was ~3.09 ps. From the trace obtained by using the background-free setup B [Fig. 9(b)] we determined τ_p to be approximately 3.04 ps, agreeing well with the previous result. Looking at background-free autocorrelation, we notice that while the wings of the trace approach zero, the finite modal contrast of ~23 dB causes residual interference fringes. Further suppression of these fringes should be possible when mode multiplexers with increased contrast are used; contrast ratios approaching 30 dB have already been demon-

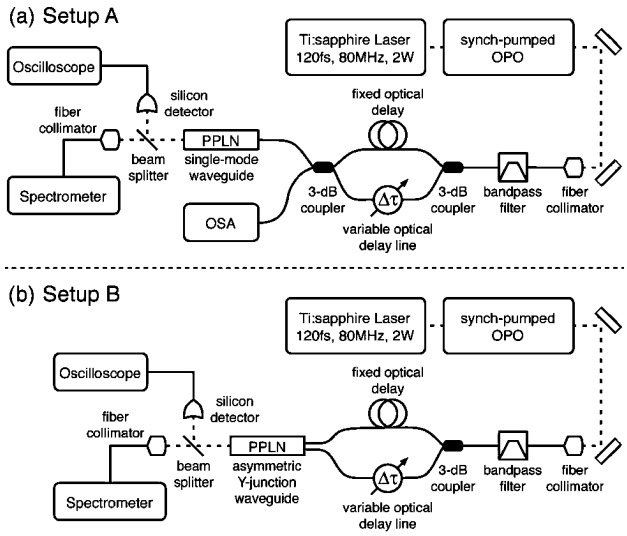

Fig. 8. Schematic of experimental setup used for autocorrelation and FROG measurements. Setup A contains a single-mode A-PPLN waveguide, while setup B contains a mode-multiplexing waveguide structure.

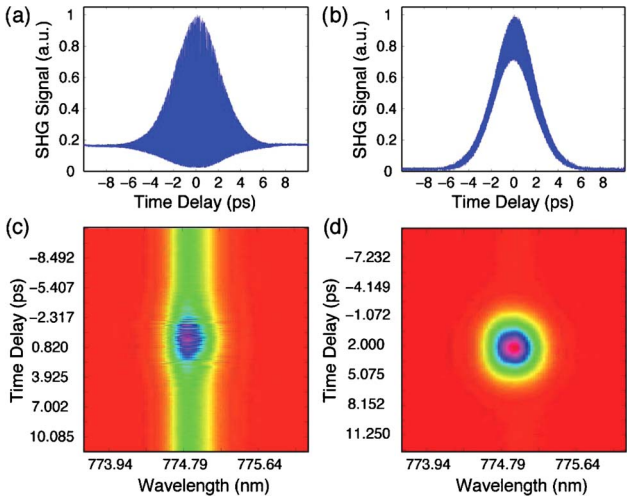

Fig. 9. (Color online) Interferometric (a) autocorrelation and (c) FROG trace obtained using setup A. Background-free collinear (b) autocorrelation and (d) FROG trace obtained using setup B.

strated [49]. In practice, these fringes do not interfere with the FROG measurements and will be averaged out if the spectrometer's integration time is long compared with the rate of delay change. For example, the data shown in Fig. 9(a) and 9(b) were obtained by sweeping the delay line with 1 ps/s across a 20 ps delay range.

Using the spectrometer (~0.025 nm resolution), set to integrate for 10 ms and average over five consecutive traces, we recorded the SHG/SFG spectra as a function of temporal delay across a 40 ps delay range, sweeping the delay with 0.25 ps/s. Shown in Fig. 9(c) is the FROG trace obtained using setup A, while the one in Fig. 9(d) was taken with setup B. Suppression of the background SH components in setup B significantly reduced the data offset, while the reduction in interference improved its smoothness.

Using a commercial SHG FROG retrieval algorithm (Femtosoft FROG), we retrieved the spectrum and temporal profile (Fig. 10) of the pulse represented by the FROG trace shown in Fig. 9(d) with good accuracy (FROG error <0.0009). The software estimated the spectral FWHM to be 1.13 nm and the temporal FWHM to be 3.168 ps, with a FWHM time–bandwidth product of 0.45.

7. POLARIZATION INSENSITIVE ULTRALOW-POWER SHG FROG

Sections 4–6 discussed ultralow-power SHG FROG with three kinds of A-PPLN waveguides. Since the waveguides

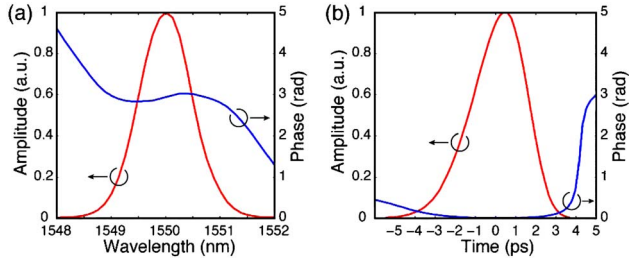

Fig. 10. (Color online) Calculated (a) spectral and (b) temporal amplitude and phase information using a retrieval algorithm.

support only a single polarization (as described in Section 3) and the SH efficiency is in general strongly polarization dependent, fluctuations of the input state of polarization (SOP) arising from the small birefringence of optical fibers in the measurement loop will seriously degrade the FROG measurement. In previous measurements, we carefully controlled the input SOP and attempted to eliminate polarization fluctuations by carefully taping all the fibers to the optical table. However, SOP fluctuations are very difficult to avoid in optical fiber loops of any significant distance, even for distances of only a few tens of meters, as are typical for connecting different optical tables. Effects are even more serious for actual fiber communications applications, where much longer fibers are used. Here, we describe a polarization-insensitive measurement technique that overcomes the polarization sensitivity of SHG FROG by scrambling the input SOP at a rate much faster than the measurement integration time [22].

The SHG FROG trace for the electric field $E(t)$ with a stationary SOP is given by Eq. (1). In the case of a frequency-independent but slowly time-varying SOP, the electric field can be expressed in Jones vector form as $E(t,t_s)=[\alpha(t_s)a(t)\ \beta(t_s)a(t)]^T$, where $|\alpha(t_s)|^2+|\beta(t_s)|^2=1$. Here t_s is a slow time variable that keeps track of the polarization variations, and t is the fast time variable over which the pulse itself varies. Since the A-PPLN waveguide supports only extraordinary-polarized light, which is TM-polarized light in z-cut substrates, the corresponding FROG trace is $I_{\mathrm{FROG}}(\Omega,\tau)=|\int dt a(t)a(t-\tau)\beta(t_s)\beta(t_s-\tau)e^{-j\Omega t}|^2$. Since in general the duration of the pulses under test is less than a few picoseconds $\beta(t_s)=\beta(t_s-\tau)$. The measured spectrum at each time delay τ will be the superposition of the spectra of all the pulses within the measurement integration time (800 ms in our experiments). Under normal laboratory conditions, the polarization fluctuation rate induced by optical fibers is of the order of several seconds, while the FROG measurement takes several minutes. The fluctuations will therefore introduce random power modulations onto the spectrograms taken at different τ, which degrades the accuracy of the FROG measurement. By scrambling the polarization states of the electric field uniformly on the Poincaré sphere at a speed much faster than the measurement integration time, the magnitude of $|\beta|^2$ within the measurement integration time can be represented by a uniform distribution. By calculating the expectation value of $|\beta|^4$, one obtains the time-polarization-averaged FROG trace. This turns out to be the same as the FROG trace of a pulse with stationary SOP, except that the power is reduced by a factor of 1/3:

$$I_{\mathrm{FROG\text{-}Scrambled}}(\Omega,\tau)=\frac{1}{3}\left|\int dt a(t)a(t-\tau)e^{-j\Omega t}\right|^2. \quad (5)$$

Equation (5) indicates that fast polarization scrambling can average out the impairments on a FROG trace induced by slow polarization fluctuations. Note that we assumed the polarization fluctuations to be frequency independent. This assumption is valid except when the fibers in the measurement are very long and polarization mode dispersion causes frequency-dependent polarization fluc-

tuations. To give an example, given a pulse width of several hundred femtoseconds, a 1 km long stretch of SMF (0.05 ps/km$^{1/2}$ assumed) will not introduce significant frequency-dependent polarization fluctuations.

Figure 11 shows the polarization-insensitive FROG setup. The setup is basically the same as the one in Section 5, except that we placed a wideband fiber-pigtailed polarization scrambler with a greater than 100 nm operating range centered at 1550 nm and 700 kHz scrambling frequency (General Photonics Corporation, PCD-104) between the input and the Michelson interferometer. As described in Section 5, the input signal consisted of nearly bandwidth-limited ~360 fs pulses at a 50 MHz repetition rate and 1550 nm center wavelength. To enhance the polarization fluctuation effects, we randomly adjusted the SOP from the source by hand, using a polarization controller (PC). We first performed the FROG measurement with the scrambler off, using a maximum of 19 nW average power coupled into the waveguide. Figure 12 shows the measurement results. The measured FROG trace exhibits random power fluctuations with time, and the retrieved FROG trace differs significantly from the measured one. Furthermore, the retrieved spectrum does not agree with the spectrum measured independently by using an optical spectrum analyzer (OSA). All of these observations indicate severe problems with the measurement.

We then repeated this experiment with the scrambler on, while continuing to randomly adjust the input SOP. The measurement was performed at an average coupled input power of 5.2 nW. Note that by finding the expectation value of $|\beta|^2$, the measured average power of the fundamental harmonic signal with the scrambler turned on is 1/2 of the power with the scrambler turned off and the input SOP optimized for maximum coupling. Figure 13 shows the measurement results. The measured FWHM was 352 fs, very close to that of the input pulses. The retrieved spectrum was very close to that measured by using the OSA, and the FROG error was 0.0047, indicating a properly performing pulse measurement. The above described polarization-insensitive technique completely eliminates the degradation of the FROG measurement induced by frequency-independent SOP fluctuation.

8. CHROMATIC DISPERSION AND ALL-ORDER PMD COMPENSATION WITH SHG FROG

In this section, we apply the proposed FROG techniques to high-order dispersion compensation and all-order PMD

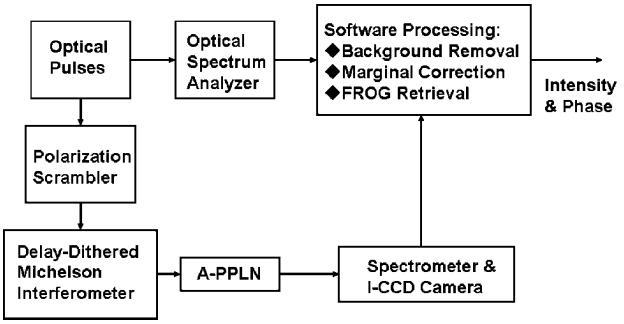

Fig. 11. Scheme of polarization-insensitive FROG.

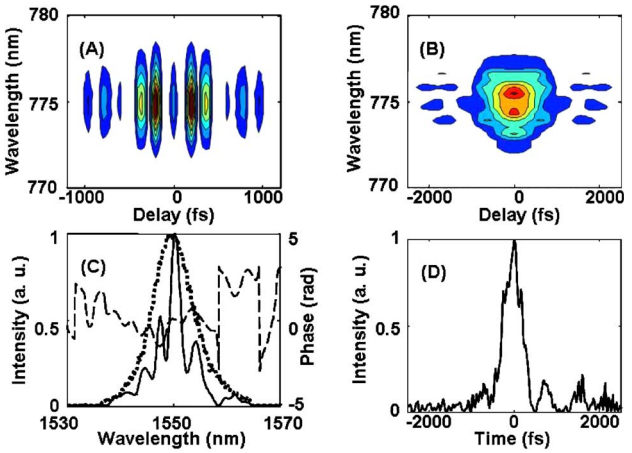

Fig. 12. (Color online) FROG data with time-varying polarization fluctuations intentionally introduced and scrambler off. (A) Measured FROG trace. (B) Retrieved FROG trace. (C) Retrieved spectral intensity (solid) and phase (dashed) profiles together with the spectrum recorded by OSA (dotted). (D) Retrieved temporal intensity profile.

compensation experiments. PMD is considered to be one of the major obstacles for the development of ultrahigh-capacity telecommunication systems [53]. PMD arises from the random birefringence in SMF owing to the imperfection in the cylindrical symmetry of the fiber cross section. This results in a time-stochastic and wavelength-dependent variation of the SOPs and delays, which degrade the system capacity. Our group demonstrated for the first time (to our knowledge) experimental wideband all-order PMD compensation by applying ultrafast pulse-shaping techniques [23]. We first rotated the distorted SOP spectra to a fixed linear state on a wavelength-by-wavelength basis via a specially designed SOP pulse shaper [54] and then applied the inverse of the estimated spectral phase via a phase-only pulse shaper. In our group's early work, the spectral phase was obtained by measuring the temporal intensity profile via cross correlation, measuring the spectrum by using an optical spectrum analyzer, and then applying the Gerchberg–Saxton

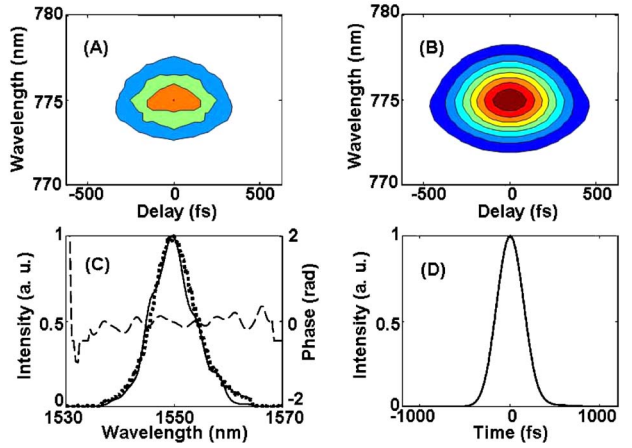

Fig. 13. (Color online) FROG data with time-varying polarization fluctuations intentionally introduced and scrambler on. (A) Measured FROG trace. (B) Retrieved FROG trace. (C) Retrieved spectral intensity (solid) and phase (dashed) profiles together with the spectrum recorded by OSA (dotted). (D) Retrieved temporal intensity profile.

algorithm [55]. However, because of the complexity of the all-order PMD-induced pulse distortion and due the limits of the Gerchberg–Saxton algorithm, an iterative measure-compensate-measure procedure was necessary, which lacked the robustness that will be needed for real-world applications. Here, we demonstrate that our ultra-low-power SHG FROG technique can accurately retrieve the extremely complex electrical field distorted by all-order PMD effects [24,25].

The experimental setup for high-order dispersion compensation and compensation of all-order PMD-induced distortion at selected polarization slices is shown in Fig. 14. The input signal is nearly bandwidth-limited ~360 fs pulses at a 50 MHz repetition rate and 1550 nm center wavelength. The pulses are relayed into a fiber-coupled phase-only pulse shaper (same as in Section 5). The output of the pulse shaper is launched into the pulse distortion elements. Since the pulse distortion elements introduce not only spectral phase but also frequency-dependent polarization rotation, we place two PCs before and after the elements and use a polarizer to select some well-shaped spectra for FROG measurement. The measured spectral phase was corrected via the pulse shaper for the distortion correction.

In the high-order chromatic dispersion compensation experiments, the distortion element consists of ~50 km SMF (PMD coefficient, 0.1 ps/km$^{1/2}$) and a dispersion-compensating fiber module (OFS Fitel). Full second-order and partial third-order dispersion is compensated by the dispersion-compensating fiber. In addition to chromatic dispersion, the SMF–dispersion-compensating-fiber link also exhibits PMD with a mean differential group delay of ~700 fs, which is ~2 times the pulse width. The PMD is large enough to induce a significant frequency-dependent polarization, keeping us from using the polarization-insensitive SHG FROG scheme described above. By using the two PCs and a polarizer, we select a well-behaved spectrum for the dispersion compensation experiment. As a result of the PMD-induced frequency-dependent SOP, the FWHM of the spectrum is narrowed from 8.4 to 6.2 nm after the polarizer. Figure 15 shows the measurement results of the distorted pulses. Distortions due to cubic spectral phase are clearly visible. The inverse of the measured spectral phase is applied via the pulse shaper to precompensate for the high-order dispersion. Figure 16 shows the results after high-order dispersion compensation. The cubic spectral phase is fully compensated. The oscillating tails in the time-domain intensity profile are suppressed, and the pulses are compressed

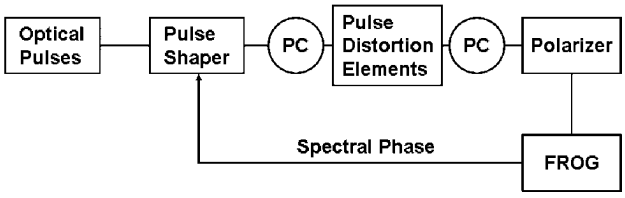

Fig. 14. Experimental setup for pulse distortion corrections controlled via SHG FROG. In the high-order dispersion compensation experiment, the pulse distortion element is 50 km SMF; in the experiment of sensing and compensation of PMD-induced pulse distortion at selected polarization slices, the distortion element is a PMD emulator. PC, polarization controller.

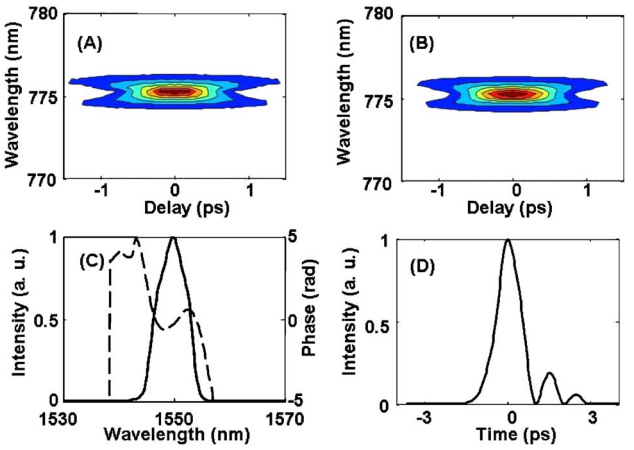

Fig. 15. (Color online) FROG data of pulses distorted by high-order chromatic dispersion. (A) Measured FROG trace. (B) Retrieved FROG trace. (C) Retrieved spectral intensity (solid) and phase (dashed) profiles. (D) Retrieved temporal intensity profile.

from 978 to 628 fs. The residual pulse broadening is due to two factors: (1) the spectrum is narrowed by PMD, and (2) the PMD-induced spectral phase varies randomly within the interval of the dispersion compensation experiment.

In the experimental setup of detection and compensation of all-order PMD-induced pulse distortion at selected polarization states, the distortion element is a homemade all-order PMD emulator consisting of eight polarization-maintaining fibers with an estimated mean differential group delay of ~1.3 ps. The goal of the experiment was to demonstrate that the proposed ultralow-power SHG FROG technique had the capability of retrieving extremely complicated waveforms resulting from all-order PMD-induced distortions. Since the average differential group delay (~1.3 ps) of the PMD module is much greater than the pulse width, strong all-order PMD effects are present, which cause complicated variations of the SOP with frequency. This leads to a reshaping of the spectrum after the polarizer. With two PCs placed before and after the PMD module and a polarizer, we can select arbitrary polarization slices for spectral phase characterization and

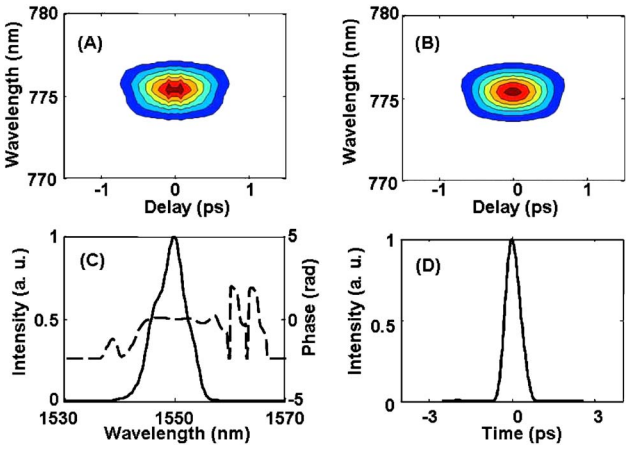

Fig. 16. (Color online) FROG data after dispersion compensation. (A) Measured FROG trace. (B) Retrieved FROG trace. (C) Retrieved spectral intensity (solid) and phase (dashed) profiles. (D) Retrieved temporal intensity profile.

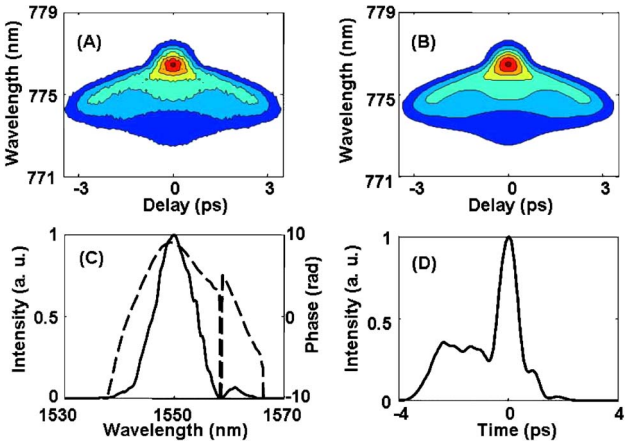

Fig. 17. (Color online) FROG data of chromatic dispersion and all-order PMD-distorted pulses at a selected polarization slice. (A) Measured FROG trace. (B) Retrieved FROG trace. (C) Retrieved spectral intensity (solid) and phase (dashed) profiles. (D) Retrieved temporal intensity profile.

correction. In our initial experiment the chromatic dispersion of the PMD module is not precompensated. The phase correction is run in precompensation mode. The same results can be achieved in postcompensation mode.

Figure 17 shows the FROG data of the chromatic dispersion and PMD-distorted pulse at a selected polarization slice. The quadratic spectral phase is caused mainly by the chromatic dispersion, while the complexity of the pulse in the time domain is due to all-order PMD. Figure 18 shows the FROG data after application of the inverse of the measured spectral phase via the pulse shaper. The pulse is compressed from more than 3 ps (at 10% intensity level) in duration to 484 fs (FWHM), which is close to the bandwidth limit. Both PMD and chromatic-dispersion-induced distortions are almost completely compensated.

We kept the applied spectral phase with the phase-only pulse shaper and adjusted the input and output PCs to select another polarization slice. In this case, the chromatic dispersion had been fully compensated in the previous trial. The observed pulse distortion was caused by the difference between the PMD-induced spectral phases (PMD-

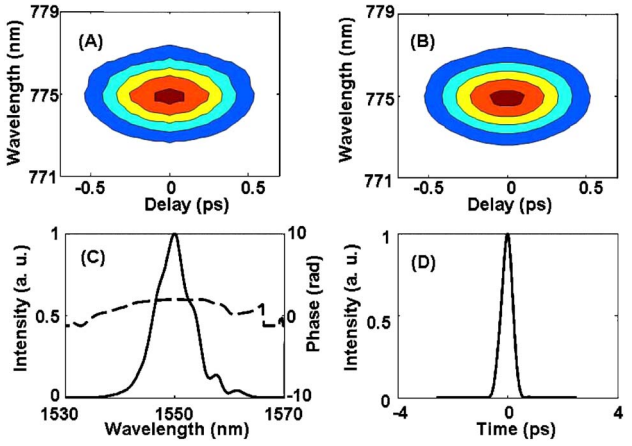

Fig. 18. (Color online) FROG data after spectral phase correction. (A) Measured FROG trace. (B) Retrieved FROG trace. (C) Retrieved spectral intensity (solid) and phase (dashed) profiles. (D) Retrieved temporal intensity profile.

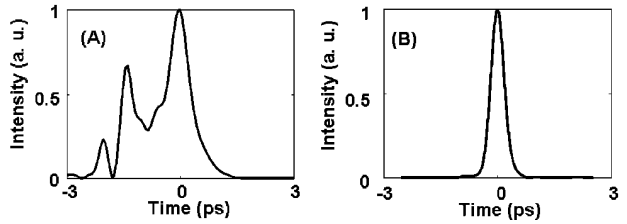

Fig. 19. Temporal intensity profiles of the (A) distorted and (B) restored pulses.

induced pulse distortion are polarization dependent) of the two experimental trials. The temporal intensity profiles of the distorted and restored pulses are shown in Fig. 19. The pulse is stretched to about 2 ps by PMD and compensated to a bandwidth-limited pulse of 400 fs.

It is worth noting that PMD-induced spectral reshaping after the polarizer accounts for the small pulse-width differences between the initial pulse and the pulses after correction, while the FROG retrieval algorithm accounts for the slight differences of the spectra before and after compensation. Since spectral phase plays the primary role in pulse distortion, the slight difference in retrieved spectra is not a significant problem.

By adjusting the PCs before and after the PMD module, we carried out the experiments several times. Each time, after correcting the PMD-induced spectral phase, we were able to obtain nearly bandwidth-limited pulses, which demonstrates the applicability of FROG measurements of PMD-distorted pulses.

We then demonstrated full all-order PMD compensation using polarization-insensitive ultralow-power SHG FROG for spectral phase sensing. Figure 20 shows the experimental setup. The SOP pulse shaper (shaper 1) and the spectral phase pulse shaper (shaper 2) are located on different optical tables. We use a pulse source (different from the previously used) located on the same table as the SOP shaper to produce ~600 fs optical pulses (~5 nm FWHM in the spectral domain) with an ~50 MHz repetition rate and 1550 nm center wavelength. The pulses were launched into the homemade PMD emulator (the same as that previously used). The SOP of the output spectrum was measured with a broadband polarimeter developed in our laboratory [56]. We used a specially designed SOP pulse shaper to correct the output SOP spectrum to the horizontal linear polarization state on a wavelength-by-wavelength basis. The liquid-crystal modulator array in the SOP shaper consists of two individually controllable 128-element layers with +90° and −45° orientations. By applying appropriate retardations, one can independently rotate any SOP point on the Poincaré sphere to the horizontal polarization state. The pulses after SOP correction were then input into a second

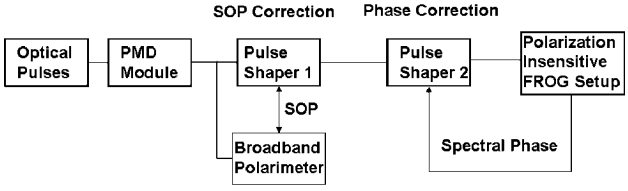

Fig. 20. Experimental setup for all-order PMD compensation.

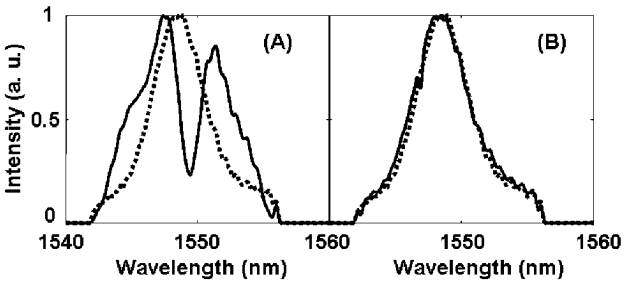

Fig. 21. Spectra (A) before and (B) after SOP correction. Solid, with PMD; dotted, without PMD.

phase-only pulse shaper. Since a 20 m long SMF is used to connect the two pulse shapers, we applied the proposed polarization-insensitive FROG technique to measure the pulses after the second shaper. By using the FROG data to control the phase-only shaper, we achieved full PMD compensation.

To check the performance of the SOP correction, we placed a polarizer after pulse shaper 1 and measured the spectra after the polarizer with and without SOP correction and compared them with the initial spectrum without PMD. Figure 21 shows one of the measurement results. The spectrum is heavily distorted by PMD and is corrected to close to the initial spectrum after SOP correction, which signifies good accuracy of the SOP measurement and correction. The peak intensity of each spectrum has been normalized to 1.

Figure 22 shows FROG data of the optical pulses after SOP correction but before spectral phase correction of one of the experimental trials. The pulses are spread to more than 3 ps (full width at 10% intensity). By applying the inverse of the measured spectral phase, the pulses are compressed to nearly bandwidth-limited 642 fs pulses as shown in Fig. 23. This is evident from the FROG traces, which are now essentially without structure, and from the flat measured spectral phase profile, as well as from the profile in the time domain. By adjusting the input SOP to the PMD emulator with a PC, we carried out the PMD compensation experiments several times. Each time we were able to compensate the pulses to similar nearly bandwidth-limited ~600 fs pulses immediately after the

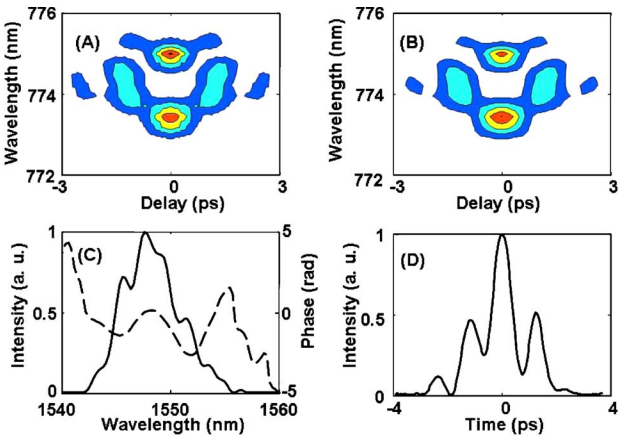

Fig. 22. (Color online) FROG data of optical pulses after SOP correction. (A) Measured FROG trace. (B) Retrieved FROG trace. (C) Retrieved spectral intensity (solid) and phase (dashed) profiles. (D) Retrieved temporal intensity profile.

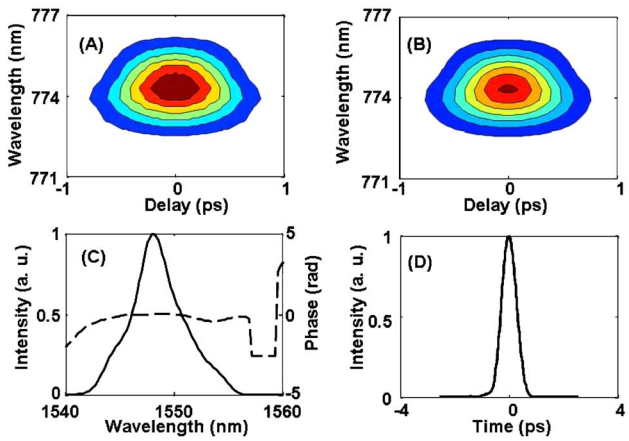

Fig. 23. (Color online) FROG data of optical pulses after SOP and spectral phase correction. (A) Measured FROG trace. (B) Retrieved FROG trace. (C) Retrieved spectral intensity (solid) and phase (dashed) profiles. (D) Retrieved temporal intensity profile.

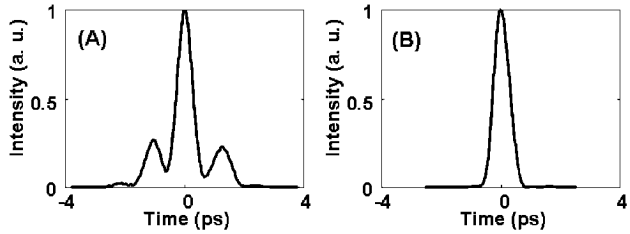

Fig. 24. Pulses (A) before and (B) after spectral phase correction.

SOP and phase-correction process. Figure 24 shows the temporal intensity profiles of the distorted (after SOP correction but before phase correction) and restored (after phase correction) pulses of another experimental trial, where the pulse is compressed to 622 fs after PMD compensation. The experimental results indicate that the proposed polarization-insensitive SHG FROG technique is robust in retrieving PMD-distorted waveforms.

9. CONCLUSION

We have reviewed ultralow-power SHG FROG using various A-PPLN waveguides, including free-space, fiber-pigtailed, and asymmetric Y-junction A-PPLN waveguides. Our experiments achieve a measurement sensitivity of 2.0×10^{-6} mW^2, ~5 orders of magnitude better than the most sensitive FROG measurements previously reported. We have also demonstrated a polarization-insensitive SHG FROG technique, which is important for practical applications involving fiber optics. Finally, we have applied these FROG measurements to control chromatic dispersion compensation and PMD compensation experiments, resulting in full correction of the impairments suffered by subpicosecond pulses in passing through optical fibers. These measurements also serve to confirm the ability to accurately retrieve extremely complicated waveforms. The ideas presented here, which involve A-PPLN engineering to obtain an optimum bandwidth–sensitivity trade-off for ultrashort pulse measurement, is also relevant to other waveform character-

ization techniques based on second-order nonlinear media, such as SPIDER and time-lens methods [57].

ACKNOWLEDGMENTS

The authors thank D. E. Leaird, L. Xu, and M. Akbulut for their contributions to experiments at Purdue and K. R. Parameswaran for providing free-space-coupled A-PPLN samples in the early phases of this collaboration. This work was supported in part by the National Science Foundation under grants 0401515-ECS and 0501366-ECS, the Air Force Office of Scientific Research (AFOSR grant FA9550-05-1-0180), the Department of Energy through Lawrence Livermore National Laboratory (DOE Prime W-7405-ENG-48), and Crystal Technology, Inc.

REFERENCES

1. X. G. Xu, S. O. Konorov, S. Zhdanovich, J. W. Hepburn, and V. Milner, "Complete characterization of molecular vibration using frequency resolved gating," J. Chem. Phys. **126**, 091102 (2007).
2. N. Belabas and M. Joffre, "Visible-infrared two-dimensional Fourier-transform spectroscopy," Opt. Lett. **27**, 2043–2045 (2002).
3. A. M. Weiner, Z. Jiang, and D. E. Leaird, "Spectrally phase-coded O-CDMA," J. Opt. Netw. **6**, 728–755 (2007).
4. R. Trebino, *Frequency-Resolved Optical Gating: the Measurement of Ultrashort Laser Pulses* (Kluwer Academic, 2000).
5. K. W. DeLong, R. Trebino, and D. J. Kane, "Comparison of ultrashort-pulse frequency-resolved-optical-gating traces for three common beam geometries," J. Opt. Soc. Am. B **11**, 1595–1608 (1994).
6. T. S. Clement, A. J. Taylor, and D. J. Kane, "Single-shot measurement of the amplitude and phase of ultrashort laser pulses in the violet," Opt. Lett. **20**, 70–72 (1995).
7. J. N. Sweetser, D. N. Fittinghoff, and R. Trebino, "Transient-grating frequency-resolved optical gating," Opt. Lett. **22**, 519–521 (1997).
8. K. W. DeLong, R. Trebino, J. Hunter, and W. E. White, "Frequency-resolved optical gating with the use of second-harmonic generation," J. Opt. Soc. Am. B **11**, 2206–2215 (1994).
9. D. T. Reid, P. Loza-Alvarez, C. T. A. Brown, T. Beddard, and W. Sibbett, "Amplitude and phase measurement of mid-infrared fs pulses by using cross-correlation frequency-resolved optical gating," Opt. Lett. **25**, 1478–1450 (2000).
10. G. Taft, A. Rundquist, M. M. Murnane, I. P. Christov, H. C. Kapteyn, K. W. DeLong, D. N. Fittinghoff, M. A. Krumbugel, J. N. Sweetser, and R. Trebino, "Measurement of 10-fs laser pulses," IEEE J. Sel. Top. Quantum Electron. **2**, 575–585 (1996).
11. C. Iaconis and I. A. Walmsley, "Self-referencing spectral interferometry for measuring ultrashort optical pulses," IEEE J. Quantum Electron. **35**, 501–509 (1999).
12. P. Baum and E. Riedle, "Design and calibration of zero-additional-phase SPIDER," J. Opt. Soc. Am. B **22**, 1875–1883 (2005).
13. E. M. Kosik, A. S. Radunsky, I. A. Walmsley, and C. Dorrer, "Interferometric technique for measuring broadband ultrashort pulses at the sampling limit," Opt. Lett. **30**, 326–328 (2005).
14. A. S. Wyatt, I. A. Walmsley, G. Stibenz, and G. Steinmeyer, "Sub-10 fs pulse characterization using spatially encoded arrangement for spectral phase interferometry for direct electric field reconstruction," Opt. Lett. **31**, 1914–1916 (2006).
15. J. R. Birge, I. Ell, and F. X. Kartner, "Two-dimensional spectral shearing interferometry for few-cycle pulse characterization," Opt. Lett. **31**, 2063–2065 (2006).
16. B. C. Thomsen, D. A. Reid, R. T. Watts, L. P. Barry, and J. D. Harvey, "Characterization of 40-Gbits/s pulses using a lithium niobate modulator at 1550 nm using frequency resolved optical gating," IEEE Trans. Instrum. Meas. **53**, 186–191 (2004).
17. M. Dinu and F. Ouochi, "Amplitude sensitivity limits of optical sampling for optical performance monitoring," J. Opt. Netw. **1**, 237–248 (2002).
18. S.-D. Yang, A. M. Weiner, K. R. Parameswaran, and M. M. Fejer, "Ultra-sensitive frequency-resolved optical gating by aperiodically poled LiNbO3 waveguides at 1.5 μm," Opt. Lett. **30**, 2164–2166 (2005).
19. H. Miao, A. M. Weiner, S. Yang, C. Langrock, R. V. Roussev, and M. M. Fejer, "Ultrasensitive second-harmonic generation frequency-resolved optical gating using a fiber-pigtailed aperiodically poled lithium niobate waveguide at 1.55 μm," in *Ultrafast Phenomena XV* (Springer, 2006), Part IV, pp. 157–159.
20. P.-A. Lacourt, J. M. Dudley, J.-M. Merolla, H. Porte, J.-P. Goedgebuer, and W. T. Rhodes, "Milliwatt-peak-power pulse characterization at 1.55 μm by wavelength-conversion frequency-resolved optical gating," Opt. Lett. **27**, 863–865 (2002).
21. C. Langrock and M. M. Fejer, "Background-free collinear autocorrelation and frequency-resolved optical gating using mode multiplexing and demultiplexing in reverse-proton-exchange aperiodically poled lithium niobate waveguides," Opt. Lett. **32**, 2306–2308 (2007).
22. H. Miao, A. M. Weiner, C. Langrock, R. V. Roussev, and M. M. Fejer, "Polarization insensitive ultralow-power second-harmonic generation frequency-resolved optical gating," Opt. Lett. **32**, 874–876 (2007).
23. A. M. Weiner, "Femtosecond pulse shaping using spatial light modulators," Rev. Sci. Instrum. **71**, 1929–1960 (2000).
24. H. Miao, A. M. Weiner, C. Langrock, R. V. Roussev, and M. M. Fejer, "Sensing and compensation of femtosecond waveform distortion induced by all-order polarization mode dispersion at selected polarization states," Opt. Lett. **32**, 424–426 (2007).
25. H. Miao, L. Xu, A. M. Weiner, C. Langrock, R. V. Roussev, and M. M. Fejer, "Broadband all-order polarization mode dispersion compensation," in *Optical Fiber Communication Conference and Exposition and The National Fiber Optic Engineers Conference*, OSA Technical Digest Series (CD) (Optical Society of America, 2007), paper OTuN2.
26. E. P. Ippen and C. V. Shank, "Techniques for measurement," in *Ultrashort Light Pulses*, S. L. Shapiro, ed. (Springer-Verlag, 1977), pp. 85–88.
27. A. M. Weiner, "Effect of group velocity mismatch on the measurement of ultrashort optical pulses via second harmonic generation," IEEE J. Quantum Electron. **19**, 1276–1283 (1983).
28. P. O'Shea, M. Kimmel, X. Gu, and R. Trebino, "Highly simplified device for ultrashort-pulse measurement," Opt. Lett. **26**, 932–934 (2001).
29. P. O'Shea, M. Kimmel, X. Gu, and R. Trebino, "Increased-bandwidth in ultrashort-pulse measurement using an angle-dithered nonlinear-optical crystal," Opt. Express **7**, 342–349 (2000).
30. M. M. Fejer, G. A. Magel, D. H. Jundt, and R. L. Byer, "Quasi-phase-matched second harmonic generation: tuning and tolerances," IEEE J. Quantum Electron. **28**, 2631–2654 (1992).
31. G. D. Miller, R. G. Batchko, W. M. Tulloch, D. R. Weise, M. M. Fejer, and R. L. Byer, "42%-efficient single-pass CW second-harmonic generation in periodically poled lithium niobate," Opt. Lett. **22**, 1834–1836 (1997).
32. J. Huang, X. P. Xie, C. Langrock, R. V. Roussev, D. S. Hum, and M. M. Fejer, "Amplitude modulation and apodization of quasi-phase-matched interactions," Opt. Lett. **31**, 604–606 (2006).
33. G. Imeshev, M. A. Arbore, S. Kasriel, and M. M. Fejer, "Pulse shaping and compression by second-harmonic

generation with quasi-phase-matching gratings in the presence of arbitrary dispersion," J. Opt. Soc. Am. B **17**, 1420–1437 (2000).
34. G. Imeshev, M. A. Arbore, M. M. Fejer, A. Galvanauskas, M. Fermann, and D. Harter, "Ultrashort-pulse second-harmonic generation with longitudinally nonuniform quasi-phase-matching gratings: pulse compression and shaping," J. Opt. Soc. Am. B **17**, 304–318 (2000).
35. A. M. Schober, G. Imeshev, and M. M. Fejer, "Tunable-chirp pulse compression in quasi-phase-matched second-harmonic generation," Opt. Lett. **27**, 1129–1131 (2002).
36. S.-D. Yang, A. M. Weiner, K. R. Parameswaran, and M. M. Fejer, "400-photon-per-pulse ultrashort pulse autocorrelation measurement with aperiodically poled lithium niobate waveguides at 1.55 μm," Opt. Lett. **29**, 2070–2072 (2004).
37. J. L. Jackel, C. E. Rice, and J. J. Veselka, "Proton exchange for high-index waveguides in $LiNbO_3$," Appl. Phys. Lett. **41**, 607–608 (1982).
38. G. P. Bava, I. Montrosset, W. Sohler, and H. Suche, "Numerical modeling of Ti:$LiNbO_3$ integrated optical parametric oscillators," IEEE J. Quantum Electron. **23**, 42–51 (1987).
39. V. A. Ganshin, Y. N. Korkishko, and V. Z. Petrova, "Reverse ion exchange in H:$LiNbO_3$ optical waveguides," Zh. Tekh. Fiz. **58**, 1168–1170 (1988).
40. V. A. Ganshin and Y. N. Korkishko, "Some features of reverse ion exchange in H:$LiNbO_3$ optical waveguides," Sov. Phys. Tech. Phys. **35**, 1095–1096 (1988).
41. J. L. Jackel and J. J. Johnson, "Reverse exchange method for burying proton exchanged waveguides," Electron. Lett. **27**, 1360–1361 (1991).
42. J. Olivares and J. M. Cabrera, "Guided modes with ordinary refractive index in proton exchanged $LiNbO_3$ waveguides," Appl. Phys. Lett. **62**, 2468–2470 (1993).
43. M. Asobe, H. Miyazawa, O. Tadanaga, Y. Nishida, and H. Suzuki, "A highly damage-resistant Zn:$LiNbO_3$ ridge waveguide and its application to a polarization-independent wavelength converter," IEEE J. Quantum Electron. **39**, 1327–1333 (2003).
44. Y. Nishida, H. Miyazawa, A. Asobe, O. Tadanaga, and H. Suzuki, "0-dB wavelength conversion using direct-bonded QPM-Zn:$LiNbO_3$ ridge waveguide," IEEE Photon. Technol. Lett. **17**, 1049–1051 (2005).
45. Y. N. Korkishko, V. A. Fedorov, T. M. Morozova, F. Caccavale, F. Gonella, and F. Segato, "Reverse proton exchange for buried waveguides in $LiNbO_3$," J. Opt. Soc. Am. A **15**, 1838–1842 (1998).
46. M. H. Chou, M. A. Arbore, and M. M. Fejer, "Adiabatically tapered periodic segmentation of channel waveguides for mode-size transformation and fundamental mode excitation," Opt. Lett. **21**, 794–796 (1996).
47. R. V. Roussev, X. Xie, K. Parameswaran, M. M. Fejer, and J. Tian, "Accurate semi-empirical model for annealed proton exchanged waveguides in *z*-cut lithium niobate," in *Lasers and Electro-Optics Society 2003. LEOS 2003. The 16th Annual Meeting of the IEEE* (IEEE, 2003), Vol. 1, pp. 338–339.
48. R. V. Roussev, "Optical-frequency mixers in periodically poled lithium niobate: materials, modeling and characterization," Ph.D. Thesis (Stanford University, 2006).
49. J. R. Kurz, J. Huang, X. Xie, T. Saida, and M. M. Fejer, "Mode multiplexing in optical frequency mixers," Opt. Lett. **29**, 551–553 (2004).
50. X. Xie and M. M. Fejer, "Two-spatial-mode parametric amplifier in lithium niobate waveguides with asymmetric Y junctions," Opt. Lett. **31**, 799–801 (2006).
51. H. A. Haus, K. Tamura, L. E. Nelson, and E. P. Ippen, "Stretched-pulse additive pulse mode-locking in fiber ring lasers: theory and experiments," IEEE J. Quantum Electron. **31**, 591–598 (1995).
52. S.-D. Yang, H. Miao, Z. Jiang, A. M. Weiner, K. R. Parameswaran, and M. M. Fejer, "Ultrasensitive nonlinear measurements of femtosecond pulses in the telecommunications band by aperiodically poled $LiNbO_3$ waveguides," Appl. Opt. **46**, 6759–6769 (2007).
53. H. Kogelnik, R. M. Jopson, and L. E. Nelson, "Polarization mode dispersion" in *Optical Fiber Telecommunications IVB—Systems and Impairments*, I. P. Kaminow and T. Li, ed. (Academic, 2002), p. 723.
54. M. Akbulut, A. M. Weiner, P. Cronin, and P. J. Miller, "Broadband polarization correction with programmable liquid-crystal modulator arrays," Opt. Lett. **29**, 1129–1131 (2004).
55. M. Akbulut, A. M. Weiner, and P. J. Miller, "Wideband all-order polarization mode dispersion compensation via pulse shaping," Opt. Lett. **30**, 2691–2693 (2005).
56. S. X. Wang and A. M. Weiner, "A complete spectral polarimeter design for lightwave communication systems," J. Lightwave Technol. **24**, 3982–3991 (2006).
57. C. V. Bennett and B. H. Kolner, "Upconversion time microscope demonstrating 103× magnification of femtoseconds waveforms," Opt. Lett. **24**, 783–785 (1999).